

# Paleoceanography and Paleoclimatology®

## RESEARCH ARTICLE

10.1029/2025PA005217

### Key Points:

- A regional carbon cycle model shows that geologic carbon release can explain extreme radiocarbon depletion in the eastern tropical Pacific
- Neutralized carbon release matches observations without significantly lowering pH or causing calcium carbonate dissolution
- Localized geologic carbon inputs can produce strong regional radiocarbon anomalies without requiring changes in large-scale ocean circulation

### Supporting Information:

Supporting Information may be found in the online version of this article.

### Correspondence to:

R. A. Green,  
[rygreen@ucsc.edu](mailto:rygreen@ucsc.edu)

### Citation:

Green, R. A., Rafter, P. A., Sun, C., Gray, W. R., Rae, J. W. B., Pelly, M., et al. (2026). Simulating deglacial radiocarbon anomalies with pH-neutral geologic carbon. *Paleoceanography and Paleoclimatology*, 41, e2025PA005217. <https://doi.org/10.1029/2025PA005217>


Received 3 JUN 2025  
Accepted 21 OCT 2025

### Author Contributions:

**Conceptualization:** P. A. Rafter, M. P. Hain  
**Data curation:** P. A. Rafter, W. R. Gray, J. W. B. Rae, M. Pelly, C. Xu, K. Thirumalai, J. R. Southon  
**Formal analysis:** P. A. Rafter, W. R. Gray, J. W. B. Rae, M. Pelly, C. Xu, K. Thirumalai, J. R. Southon  
**Funding acquisition:** P. A. Rafter, M. P. Hain  
**Methodology:** P. A. Rafter, W. R. Gray, J. W. B. Rae, M. Pelly, C. Xu, K. Thirumalai, J. R. Southon, M. P. Hain  
**Software:** C. Sun, M. P. Hain  
**Supervision:** P. A. Rafter, M. P. Hain  
**Writing – original draft:** C. Sun, M. P. Hain  
**Writing – review & editing:** P. A. Rafter, C. Sun, W. R. Gray, J. W. B. Rae, M. Pelly, C. Xu, K. Thirumalai, F. Pavia, M. P. Hain

© 2026. American Geophysical Union. All Rights Reserved.

## Simulating Deglacial Radiocarbon Anomalies With pH-Neutral Geologic Carbon

R. A. Green<sup>1,2</sup> , P. A. Rafter<sup>3</sup> , C. Sun<sup>4</sup> , W. R. Gray<sup>5</sup> , J. W. B. Rae<sup>6</sup> , M. Pelly<sup>6</sup> , C. Xu<sup>6</sup> , K. Thirumalai<sup>7</sup> , J. R. Southon<sup>8</sup> , F. Pavia<sup>9</sup> , and M. P. Hain<sup>1</sup> 

<sup>1</sup>Earth and Planetary Sciences Department, University of Santa Cruz, Santa Cruz, CA, USA, <sup>2</sup>Equatic, Torrance, CA, USA, <sup>3</sup>College of Marine Science, University of South Florida, St. Petersburg, FL, USA, <sup>4</sup>Stanford University, Stanford, CA, USA, <sup>5</sup>Laboratoire des Sciences du Climat et de l'Environnement (LSCE/IPSL), Gif-sur-Yvette, France, <sup>6</sup>School of Earth and Environmental Sciences, University of St Andrews, St Andrews, UK, <sup>7</sup>Department of Geosciences, University of Arizona, Tucson, AZ, USA, <sup>8</sup>Department of Earth System Science, University of California Irvine, Irvine, CA, USA, <sup>9</sup>Department of Oceanography, University of Washington, Seattle, WA, USA

**Abstract** There is currently no explanation or carbon cycle model scenario for severe radiocarbon (<sup>14</sup>C) depletion reconstructed in the intermediate depth eastern tropical North Pacific Ocean (ETNP) at the end of the last ice age. Here, we develop new constraints on hypothesized geologic carbon release based on the boron isotope pH proxy and regional refinement of a global carbon cycle model. We find that pH-neutral release of ~800 Pg C over 5,000 years can produce the radiocarbon anomalies in the ETNP while inducing neither a large pH anomaly nor CaCO<sub>3</sub> dissolution (as observed) and causing minimal atmospheric CO<sub>2</sub> rise. Mass-balance considerations dictate that the anomalous carbon was concentrated near the geologic source in the ETNP without significantly affecting radiocarbon-based reconstructions of global ocean circulation change.

**Plain Language Summary** At the end of the last ice age, unusually low levels of radiocarbon were found in ocean waters off the west coast of Mexico. These values are too extreme to be explained by normal ocean circulation. To understand what caused them, we used computer models and chemical records from ancient marine organisms. Our results show that a release of carbon from the seafloor could explain the unusual radiocarbon signals. This release occurred in a part of the ocean that is naturally isolated, which helped trap the carbon and its signal. The carbon was released in a neutralized form, so it didn't cause ocean acidification—consistent with what scientists observe in seafloor fossils. Our findings suggest that these radiocarbon anomalies were caused by a local carbon release into an already isolated region, not by changes in global ocean circulation. This supports the continued use of radiocarbon as a tool for studying past ocean changes.

## 1. Introduction

The radioactive carbon isotope <sup>14</sup>C (radiocarbon) is a key tool for measuring the rate of carbon exchange between the atmosphere and the ocean (Bolin, 1960; Craig, 1957; Revelle & Suess, 1957) and thus provides a powerful constraint on the hypothesis that deep ocean circulation changes drove the abrupt rise in atmospheric carbon dioxide (CO<sub>2</sub>) concentrations at the end of the last ice age. In what seemed to be a breakthrough moment, Marchitto et al. (2007) found severe <sup>14</sup>C depletions (decay-corrected <sup>14</sup>C:<sup>12</sup>C ratio, expressed as Δ<sup>14</sup>C; Stuiver & Polach, 1977) in intermediate-depth waters off Baja California in the Eastern Tropical North Pacific (ETNP), potentially explaining the “mystery interval”—a period of rapid atmospheric Δ<sup>14</sup>C decline and rising CO<sub>2</sub>. Broecker and Barker (2007) proposed that abyssal ocean overturning circulation had stalled during peak glacial conditions, allowing <sup>14</sup>C-depleted carbon to accumulate at depth, which was later released during the deglaciation. Subsequent radiocarbon reconstructions and data compilations confirm that deep ocean circulation slowed during the Last Glacial Maximum (LGM) and accelerated during deglaciation, supporting its role in ocean CO<sub>2</sub> release (Rafter et al., 2022; Skinner et al., 2010).

However, the ocean <sup>14</sup>C depletions discovered by Marchitto et al. (2007) were found to be too severe and prolonged to be explained by changes in global ocean overturning (Hain et al., 2011). Radiocarbon anomalies have since been reported not only across the Eastern Pacific (Bova et al., 2018; Lindsay et al., 2015; L. Stott et al., 2009, 2019; L. D. Stott et al., 2019), but also in the South Pacific (Ronge et al., 2016), the Northwestern Indian Ocean (Bryan et al., 2010) and the North Atlantic (South Iceland Basin and Nordic Seas; Thornalley et al., 2011, 2015).

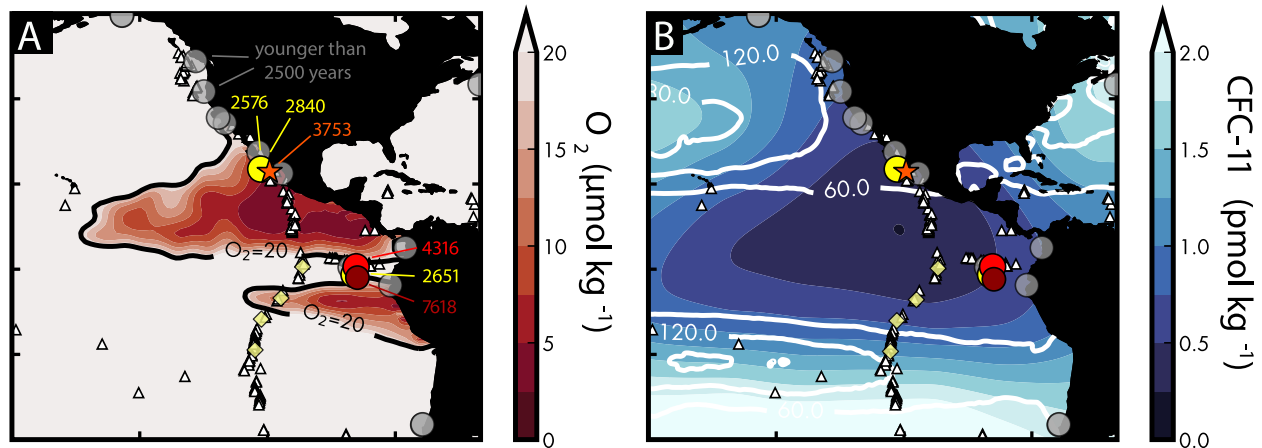


**Figure 1.** Intermediate depth (<1,000 m)  $^{14}\text{C}$  anomalies (colored points: Bova et al., 2018; Marchitto et al., 2007; Rafter et al., 2018, 2019; L. Stott et al., 2009, 2019; L. D. Stott et al., 2019) in the context of modern Eastern Pacific hydrographic conditions. Anomalies are defined as having mean deglacial (18 kyr BP–12 kyr BP) ventilation ages >2,500 years, with data collected from the Rafter et al. (2022)  $^{14}\text{C}$  compilation. The age of each anomaly record is shown in the plot. Non-anomalous  $^{14}\text{C}$  data is shown in gray. The star marks the site of new data presented in this study. Subplot (a) shows dissolved  $\text{O}_2$  ( $\mu\text{mol kg}^{-1}$ ) at 500 m depth (Garcia et al., 2023), while (b) shows concentrations of chlorofluorocarbons (CFC-11 in  $\text{pmol/kg}$ ) and white contours of potential vorticity ( $10^{-12} \text{ m}^{-1} \text{ s}^{-1}$ ) at 500 m depth (Lauvset et al., 2024). Both maps indicate the locations of hydrothermal vents, represented by white triangles. Yellow diamonds mark East Pacific Rise core sites which document elevated hydrothermal metal fluxes during the deglaciation (Frank et al., 1994; Lund et al., 2016, 2019).

Yet, there remains a particular spatial cluster of anomalies in the ETNP (Lindsay et al., 2016; Marchitto et al., 2007; Rafter et al., 2018, 2019) that have passed tests for species-specific offsets, age model biases, and the impacts of bioturbation (Rafter et al., 2018) (Figure 1). These sites exist alongside equatorial-located records that show no such anomalies (Bova et al., 2018; Chen et al., 2020), raising a significant problem for the paleoceanographic research community: if ocean circulation did not cause the radiocarbon anomalies, how reliable are radiocarbon-based reconstructions of ocean circulation?

One proposed solution is that the anomalies are due to unspecified diagenetic overprints erasing the primary seawater radiocarbon signature. However, the sampled benthic and planktonic foraminifera data in the ETNP pass a wide range of preservation tests, show replication on multiple benthic foraminifera species, and are built on a high-quality sedimentary age model (based on  $^{14}\text{C}$ -dated terrestrial wood fragments; Rafter et al., 2018)

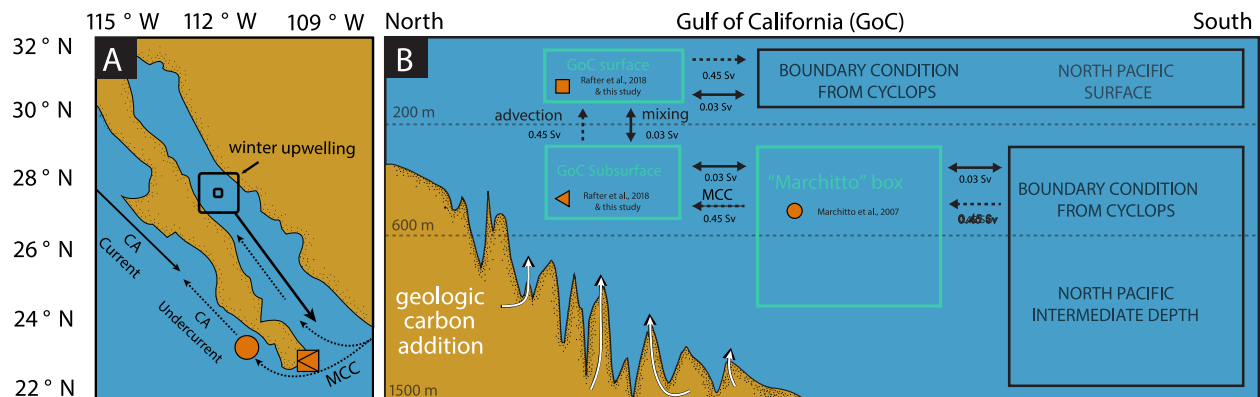


**Figure 2.** Regional model framework and observational data used to inform the model. Mean Gulf circulation is estuarine: in at depth and out at the surface (dashed arrows; Lavín & Marinone, 2003). The regional model framework is shown by the teal boxes (panel b). The model's boundary conditions come from the global carbon cycle model, CYCLOPS, and are shown with black boxes (panel b). Markers indicate the location of proxy data used in this study, from the California Undercurrent (orange circle) and Gulf of California (orange sideways triangle and square) site LPAZ-21P (a, b). In panel (b), the markers are shown in each box corresponding to which data informs which box in the regional model. In panel a, there are two markers for the Gulf of California site LPAZ-21P because the core site includes planktic and benthic data. Note that the subsurface (200 to  $\approx$ 700 m) Mexican Coastal Current (MCC) feeds into the deep Gulf and California Undercurrent (Gómez-Valdivia et al., 2015), bathing both the Gulf and Undercurrent core sites (Marchitto et al., 2007), thus the Undercurrent core site (orange circle) can be assumed representative of water “upstream” to the Gulf of California core site. Figure is adapted from Rafter et al. (2019).

(Figure 3d). One specific concern is the possibility of overgrowth of authigenic carbonate on foraminiferal tests, associated with sediment porewater sulfate reduction horizons, which can alter foraminifera  $^{14}\text{C}$  ages in northwest Pacific sediments (Cook et al., 2011). If these  $\Delta^{14}\text{C}$  anomalies were driven by sulfate reduction, we would expect them at similar sediment depths along the same redox horizon. Instead, the anomalies are found in sediments of the same geological age but at varying depths (Marchitto et al., 2007; Rafter et al., 2018). This coincidence could be explained by active sulfate reduction in surface mixed-layer sediments during the anomalous periods, possibly driven by transient intensification of oxygen-deficient denitrification zones in the eastern tropical Pacific during the deglacial period (Studer et al., 2021). However, a dilution of foraminiferal calcite greater than 20% needed to produce a 200‰ radiocarbon anomaly would be visible upon inspection of the picked foraminiferal samples and moreover, their stable isotopic composition would reveal the poor preservation state of the tests—neither of which are observed (Cook & Keigwin, 2015; Rafter et al., 2018). As such, we lack any sound basis to discount the ETNP radiocarbon anomalies, posing a challenge to interpreting other spatially isolated deglacial radiocarbon anomalies, such as those offshore Oman (Bryan et al., 2010) and the Galapagos (L. Stott et al., 2009).

We investigate an alternative explanation for the deglacial radiocarbon anomalies: a release of  $^{14}\text{C}$ -free carbon from geologic sources on the ETNP seafloor (Lund & Asimow, 2011; Rafter et al., 2019; Ronge et al., 2016; L. Stott & Timmermann, 2011; L. Stott et al., 2009, 2019; L. D. Stott et al., 2019), possibly related to climate-paced variability in seafloor spreading and volcanism (Huybers & Langmuir, 2009; Lund & Asimow, 2011; Lund et al., 2016, 2019). Independent evidence for enhanced hydrothermal activity during deglaciation is also provided by ridge-crest sediment records of metal fluxes along the EPR (Frank et al., 1994; Lund et al., 2016, 2019). In this hypothesized scenario, the anomalous foraminiferal samples grew in seawater with admixed geologic carbon. Some proponents of this hypothesis suggest the geologic carbon was released in the form of  $\text{CO}_2$ , contributing to the deglacial rise of atmospheric  $\text{CO}_2$  (Ronge et al., 2016; L. Stott & Timmermann, 2011; L. Stott et al., 2009, 2019; L. D. Stott et al., 2019). However, significant  $\text{CO}_2$  release would have lowered seawater pH and reduced carbonate ion ( $\text{CO}_3^{2-}$ ) concentrations and  $\text{CaCO}_3$  saturation, causing partial or complete dissolution of the anomalous foraminifera material—which instead appears well preserved (Lindsay et al., 2015; Marchitto et al., 2007; Rafter et al., 2018, 2019; L. Stott et al., 2009).

More recently, Rafter et al. (2019) proposed that the geologic carbon was instead neutralized by an equimolar amount of alkalinity, converting the  $\text{CO}_2$  to bicarbonate ( $\text{HCO}_3^-$ ) and mitigating localized seawater acidification. Such alkalinity could plausibly be supplied by carbonate mineral dissolution, consistent with the limited  $\delta^{13}\text{C}$  shift associated with neutralized geologic carbon addition (Green et al., 2024; Figure S1 in Supporting Information S1), though basalt alteration or other water–rock reactions may also have contributed. Further, inverse carbon cycle modeling based on reconstructed atmospheric  $\text{CO}_2$  and  $\Delta^{14}\text{C}$  records suggests that geologic carbon release was unlikely to exceed  $\sim 800$  Pg C and must have been accompanied by a comparable input of alkalinity (Green et al., 2024). However, this scenario fails to produce basin-scale  $\Delta^{14}\text{C}$  anomalies due to the rapid dissipation of the  $\Delta^{14}\text{C}$  signal within the global carbon cycle (Green et al., 2024; Hain et al., 2011).

In this study, we directly assimilate the anomalous ETNP  $\Delta^{14}\text{C}$  data to infer the required carbon release in a refined model representation of the Gulf of California (GoC) region with varying degrees of hydrographic isolation. We also present new benthic and planktic foraminiferal boron isotope data ( $\delta^{11}\text{B}$ , a proxy for seawater pH), measured on the same samples and over the same interval as the observed  $^{14}\text{C}$ -depletions. These data allow us to constrain the carbonate system perturbation associated with the  $^{14}\text{C}$ -depletions and determine the concomitant alkalinity inputs.

## 2. Materials and Methods

### 2.1. Model Details

#### 2.1.1. ETNP Regional Model

To simulate geologic carbon addition in the Eastern Tropical North Pacific (ETNP), we developed a regional three-box carbon cycle model specifically tailored to this region. The model comprises three connected boxes: (a) the intermediate-depth ETNP shadow zone, which interacts with the Gulf of California (GoC) via the Mexican Coastal Current (MCC; Gómez-Valdivia et al., 2015), (b) the northward-flowing subsurface GoC waters, and (c) the southward-flowing surface waters in the GoC. These are referred to as the “Marchitto box” (in reference to the original discovery of the  $\Delta^{14}\text{C}$  anomalies; Marchitto et al., 2007), the “GoC subsurface box,” and the “GoC

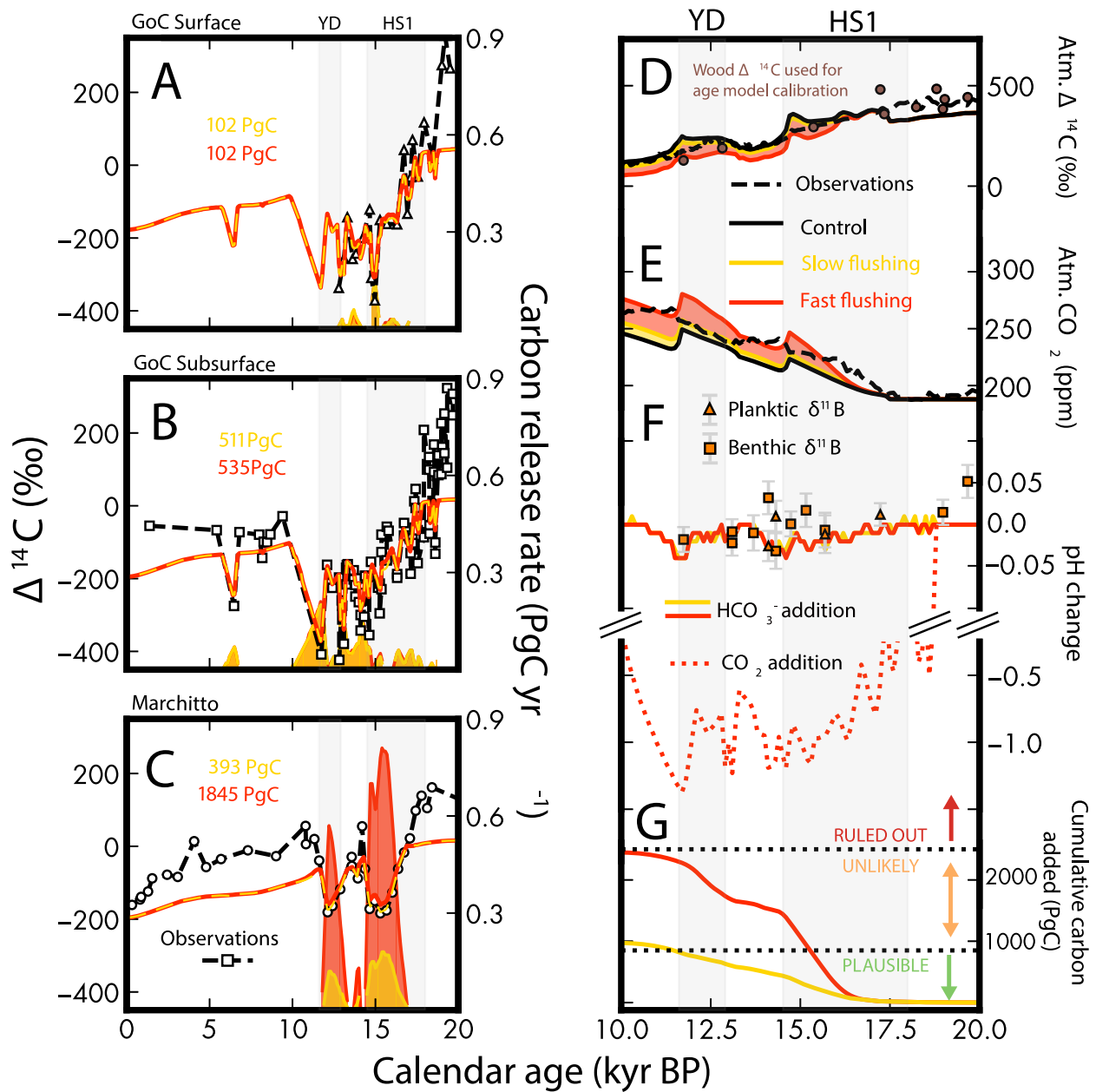


**Figure 3.** Comparison of simulated and observed  $^{14}\text{C}$  anomalies, atmospheric data, and pH change, with modeled geologic carbon release rates for both slow and fast flushing experiments. Panels (a–c) display the simulated  $\Delta^{14}\text{C}$  anomalies and release rates for the Marchitto box (panel c), the GoC subsurface (panel b) and the surface (panel a), with observational  $\Delta^{14}\text{C}$  data shown as markers: circles for the Marchitto box (Marchitto et al., 2007), squares for GoC subsurface (Rafter et al., 2018) (benthic), and triangles for GoC surface (Rafter et al., 2018; planktic). Simulated  $\Delta^{14}\text{C}$  results are shown as lines with shaded areas representing release rates. Yellow and red correspond to the slow and fast flushing experiments, respectively. Panel (d, e) display atmospheric  $\Delta^{14}\text{C}$  (Reimer et al., 2020) and  $\text{CO}_2$  (Bereiter et al., 2015), respectively, alongside simulated results. The simulated results are shown relative to a control run based on the deglacial carbon cycle scenario from Hain et al. (2014). Wood  $\Delta^{14}\text{C}$  data is shown with brown circles, which was used for calibrating the age model in Rafter et al. (2018, 2019) and the new data from this study. Panel (f) shows the observed pH change (derived from  $\delta^{11}\text{B}$  data, with  $1\sigma$  uncertainty indicated by error bars) and simulated pH change. Panel (g) displays cumulative carbon addition, with dashed black lines showing constraints based on the global radiocarbon budget (Green et al., 2024).

surface box,” respectively (Figure 2). Within these boxes we optimize for carbon and alkalinity fluxes to replicate the observed  $\Delta^{14}\text{C}$  anomalies (Marchitto et al., 2007; Rafter et al., 2018, 2019).

The GoC subsurface and surface boxes are assigned depths of 600 and 200 m, respectively, with the subsurface depth based on benthic radiocarbon records found at 624 m (Rafter et al., 2018) and the surface depth based on

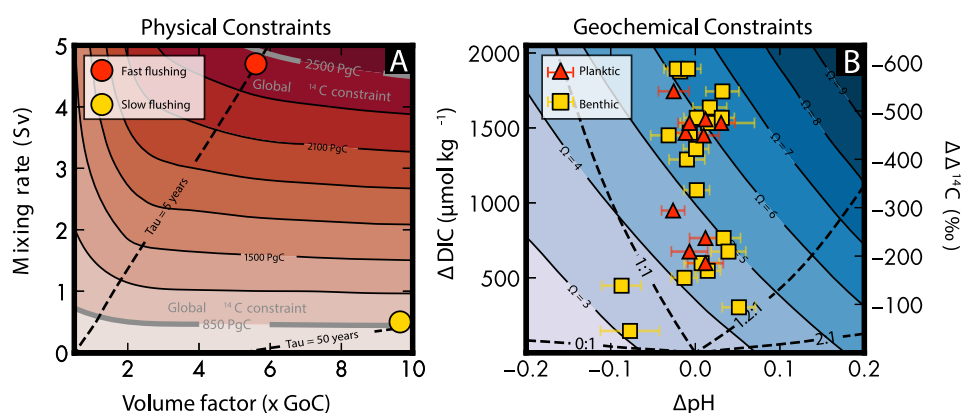


**Figure 4.** Physical and geochemical constraints on geologic carbon addition. (a) Physical constraints showing simulated carbon release across a range of mixing rates (y-axis) and Marchitto Box sizes (x-axis, in multiples of GoC volume). Contours represent the total carbon required simulate  $\Delta^{14}\text{C}$  anomalies, with gray lines indicating global radiocarbon budget limits (Green et al., 2024). Yellow and red circles denote slow and fast flushing end-member experiments, respectively, with black dashed lines showing their respective residence times of the Marchitto box. (b) Geochemical constraints based on PyCO2SYS (Humphreys et al., 2021) solver results and observations. Unlike Figure 3f, which covers the 20–10 ka interval, (b) includes the full  $\delta^{11}\text{B}$ -derived pH data set extending back to 35 ka; no interpolation was applied. We apply a scaling relationship between  $^{14}\text{C}$ -free carbon addition and resulting  $\Delta^{14}\text{C}$  anomalies from the CYCLOPS carbon cycle model ( $\Delta\Delta^{14}\text{C} = -0.31 * \Delta\text{DIC}$ ) to align PyCO2SYS-derived aragonite saturation state ( $\Omega$ ) contours with calculated  $\Delta\text{pH}$  and  $\Delta\Delta^{14}\text{C}$  from observed GoC data spanning 35–11 kyr BP (yellow squares for benthic and red triangles for planktic).  $1\sigma$  error bars are shown for the pH reconstruction derived from  $\delta^{11}\text{B}$ .  $\Omega$  contours are calculated from a range of DIC and pH values, assuming a baseline DIC concentration of  $2,150 \mu\text{mol kg}^{-1}$  and a pH of 8.07. Dashed black lines indicate ALK:DIC ratios for different hypothetical geologic carbon sources. Collectively, the  $\delta^{11}\text{B}$  and  $\Delta^{14}\text{C}$  data are consistent with an ALK:DIC ratio in the range of 1.0–1.2, similar to the constant ratio of 1 used in our simulations and the mean ratio of  $\sim 1.1$  estimated by Green et al. (2024). For all ratios in this range,  $\text{CaCO}_3$  saturation ( $\Omega$ ) increases with carbon addition, consistent with the observed preservation of foraminiferal tests.

Lavín and Marinone (2003). The northern boundary is defined at the Guaymas Basin, where upwelling occurs approximately 550 km north of the GoC core site (Rafter et al., 2019). The model's GoC box width is set to 150 km, following Nix (2013).

Given the uncertainty in the spatial extent and relative isolation of the  $^{14}\text{C}$ -depleted water mass entering the GoC, we conduct experiments across a range of Marchitto box sizes (0.01–10 times the GoC volume) and mixing rates (0.01–5 Sverdrups (Sv), where  $1 \text{ Sv} = 10^6 \text{ m}^3 \text{ s}^{-1}$ ; Figure 4a). We highlight two end-member cases: a “fast-flushing” scenario with high mixing (4.7 Sv) and a smaller box (5.6 times the GoC), and a “slow-flushing” scenario with low mixing (0.5 Sv) and a larger box (9.65 times the GoC). These scenarios capture how varying degrees of regional isolation affect the amount of carbon release needed to produce the reconstructed  $\Delta^{14}\text{C}$  signals. Within the regional model, advection is set at 0.45 Sv based on Rafter et al. (2019), correcting a typographical error in the original manuscript that reported 0.3 Sv. Mixing within the GoC is assigned a rate of 0.03 Sv, an initial estimate approximately 15 times smaller than the advection flux. Further details on model parameters can be found in Figure 2.

### 2.1.2. Coupling With CYCLOPS

To incorporate global carbon cycle dynamics, we coupled this regional model with the CYCLOPS global carbon cycle model (Green et al., 2024; Hain et al., 2011, 2014) through an iterative process of asynchronous model coupling. The control run simulates background deglacial conditions with no geologic carbon addition (Hain et al., 2014).

The regional GoC model is initially forced using CYCLOPS control simulation results, including P, DIC, ALK,  $\Delta^{14}\text{C}$ , and  $\delta^{13}\text{C}$  concentrations. Optimization of geologic carbon addition to the GoC regional model is conducted using the minimize function from the SciPy library (Virtanen et al., 2020), ensuring that simulated  $\Delta^{14}\text{C}$  values remain within a threshold of 0.1‰ of observations. Boundary fluxes diagnosed from the optimized GoC model are then applied as a forcing to the global CYCLOPS model to adjust the boundary condition for the GoC to be

consistent with the simulated carbon and alkalinity release. With each iteration of this process the models exchange outputs so as to maintain chemical and isotopic mass balance, ensuring that both regional and global carbon cycle processes are captured. The iterative process continues until the boundary fluxes and geologic carbon release converge on a stable solution, within 1 Pg C over two consecutive runs. In most simulations presented in the main text, geologic carbon is added with an equimolar amount of alkalinity (ALK:DIC ratio of 1:1, simulating bicarbonate addition) and a  $\delta^{13}\text{C}$  value of  $-2.5\text{‰}$ , based on Green et al. (2024). To explore other potential sources of geologic carbon, we also simulate the slow-flushing scenario with geologic carbon added as pure  $\text{CO}_2$  (ALK:DIC ratio of 0) and a  $\delta^{13}\text{C}$  value of  $-8.9\text{‰}$ , based on the mean  $\delta^{13}\text{C}$  of  $\text{CO}_2$  collected from hydrothermal vents in the GoC by Paduan et al. (2018) (Figure S1c in Supporting Information S1). Because the CYCLOPS control simulation underestimates baseline  $\Delta^{14}\text{C}$  in the intermediate North Pacific relative to the observations, the boundary conditions imposed on the ETNP model are slightly too low before optimization. As a result, simulated anomalies are muted compared to the data. If the baseline  $\Delta^{14}\text{C}$  were higher, a larger anomaly would be required, implying either greater isolation or higher geologic carbon fluxes. Because both regional ocean circulation and the rate of geologic carbon release influence the relationship between rate and resulting  $\Delta^{14}\text{C}$  signal, both factors will be analyzed and discussed below.

### 2.1.3. $\Delta^{14}\text{C}$ Data Assimilated With the Regional Model

Our regional model framework is informed by  $\Delta^{14}\text{C}$  data from benthic and planktic foraminifera collected at the mouth of the GoC and along the Pacific margin of Baja California. For the GoC, benthic and planktic foraminiferal data were gathered from a depth of 624 m (Rafter et al., 2019). The subsurface  $\Delta^{14}\text{C}$  record was built using benthic foraminifera species *Planulina ariminensis* and *Uvigerina* spp., both of which are good recorders of bottom water  $\Delta^{14}\text{C}$  (Rafter et al., 2018). The surface water  $\Delta^{14}\text{C}$  record was built by measuring the planktic foraminifera species *Globigerina bulloides*. For years with multiple benthic records, we used the average  $\Delta^{14}\text{C}$  value of both species to provide a representative estimate.

The GoC core site is influenced by the MCC, which transports poorly ventilated subsurface waters northward (Gómez-Valdivia et al., 2015). This current also supplies water to the California Undercurrent, overlying sediment core sites along the Pacific margin of Baja California, where the earliest deglacial  $\Delta^{14}\text{C}$  anomalies were observed (Marchitto et al., 2007). Accordingly, we use the mixed benthic foraminiferal record from California Undercurrent waters (Marchitto et al., 2007) as a proxy for conditions in the MCC and the ETNP shadow zone (i.e., the Marchitto box; see Figure 2). The GoC follows an estuarine circulation pattern, with deep inflowing seawater and surface outflow. Within this structure, benthic foraminiferal data represent the characteristics of poorly ventilated subsurface inflow from the MCC, while planktic foraminifera reflect the outflowing surface water conditions (i.e., the GoC boxes; see Figure 2).

In addition to  $\Delta^{14}\text{C}$ , we also measured  $\delta^{13}\text{C}$  and  $\delta^{11}\text{B}$  from the same sediment core as the GoC  $\Delta^{14}\text{C}$  anomalies (Rafter et al., 2018, 2019), derived from the benthic foraminifera *P. ariminensis*. These additional isotopic records provide further insights into the past carbonate chemistry and water mass characteristics of the ETNP, supplementing the  $\Delta^{14}\text{C}$  data used to inform the model.

In our framework, all  $\Delta^{14}\text{C}$  records (from the Marchitto box and the Gulf of California; Marchitto et al., 2007; Rafter et al., 2018, 2019) are assimilated to optimize the required geologic carbon release under different flushing scenarios. By contrast,  $\delta^{13}\text{C}$  and  $\delta^{11}\text{B}$  data from the Gulf of California core are not assimilated and therefore provide independent validation of the modeled carbonate system response.

## 2.2. Proxy Data

### 2.2.1. $\delta^{11}\text{B}$ Analytical Methods and $\Delta\text{pH}$ Calculations

Between 4 and 8 benthic and >50 planktic foraminifera tests were picked from the >250 mm and >125 mm size fraction for trace element and boron isotope ( $\delta^{11}\text{B}$ ) analyses. Sample preparations were carried out in a low-boron clean lab at the University of St Andrews. Samples were cleaned based on the “Mg-cleaning” oxidation procedure (Barker et al., 2003; Rae et al., 2011). An aliquot (~3% of the total sample) was taken for trace element analyses, which were performed on an Agilent 8900 ICP-MS at the University of St Andrews using matrix-matched standards. Long-term reproducibility of Mg/Ca and B/Ca using this method is 1.2% and 2.3% (2 SD),

respectively. Prior to  $\delta^{11}\text{B}$  analysis, samples were screened for potential contamination by checking various elemental ratios (B/Ca, Mg/Ca, and Al/Ca). All samples have Al/Ca ratios  $<100 \mu\text{mol/mol}$ .

Boron was separated from the sample matrix using Amberlite IRA-743 boron specific anion exchange resin. For one set of samples, the protocol followed the “column” method of Foster (2008) and Foster et al. (2013). For a subsequent set of samples, the “batch” protocol of Trudgill et al. (2024) was used, which improves the precision of  $\delta^{11}\text{B}$  analysis at low concentrations typical of foraminiferal samples. Analysis of the same standard by both techniques shows no significant offset between the techniques (Trudgill et al., 2024 and below).

$\delta^{11}\text{B}$  was measured on a Thermo Scientific Neptune plus MC-ICP-MS at the University of St Andrews, based on protocols described in Foster (2008), Rae et al. (2011), Rae (2018), but with the addition of high ohmage ( $10^{13} \Omega$ ) resistors and triplicate sample analyses (Trudgill et al., 2024; Xu et al., 2024). Samples were corrected for total procedural blank, which averaged 80 pg for the samples for through columns, and  $\sim 9$  pg for the samples analyzed by batch.

Rae et al. (2011) previously reported uncertainties of  $\pm 0.23\%$  (2 SD) for samples of  $\sim 20$  ng, increasing at smaller sample sizes. This has been improved given the developments in analyses described above (Trudgill et al., 2024). For example, a boric acid standard (ERM-AE121; Vogl & Rosner, 2012) run during these sessions at a similar concentration and under the same conditions as these samples (15–25 ppb) gave  $\delta^{11}\text{B} = 19.64 \pm 0.06\%$  (2 SD,  $n = 8$ ). However as full description and quantification of this updated method is beyond the scope of the current study, we assign conservative analytical uncertainties following the relationships in Rae et al. (2011) for the samples analyzed through columns. For the samples analyzed by batch (which improves the precision of small samples relative to columns), we assign the external standard deviation of repeated analysis of NIST 8301 Foram (spanning the sample size range of the foraminiferal samples) by this method during the analytical session ( $\pm 0.11\%$  2SD,  $n = 5$ ), which agrees with the long-term reproducibility of the method within the lab as reported by Trudgill et al. (2024) in size range spanning the samples.

Replicate purifications and measurements of NIST 8301 Foram (a dissolved carbonate standard with a composition mimicking planktic foraminifera), analyzed during the same analytical sessions as the samples, gave a value and  $\pm 2$  SD of  $14.72 \pm 0.23\%$  ( $n = 2$ ) using the columns method at 25 ppb, and  $14.63 \pm 0.11\%$  ( $n = 5$ ) at 15 ppb using the batch method. Thus, no significant difference between the methods is evident.

We reconstructed pH from the  $\delta^{11}\text{B}$  measurements using the established boron isotope-pH proxy (Zeebe & Wolf-Gladrow, 2001):

$$pH_0 = pK_B - \log_{10} \left( \frac{\delta_0 - \delta_{\text{SW}}}{\delta_{\text{SW}} - \alpha \times \delta_0 - \epsilon} \right)$$

Here,  $\epsilon$  and  $\alpha$  are the equilibrium boron isotope effect and fractionation factor (i.e., 27.2‰ and 1.0272; see Klochko et al. (2006).  $\delta_{\text{SW}}$  represents the boron isotopic composition of bulk seawater, for which we use 39.61‰, and  $\delta_0$  is the reconstructed boron isotopic composition of borate from which pH is calculated.  $pK_B$  is the borate/boric acid equilibrium constant, which is temperature and salinity dependent (Dickson, 1990). For calculating  $pK_B$ , we use mean ocean temperature reconstructions (Bereiter et al., 2018) and a constant salinity of 35 PSU.

Relative pH changes (Figures 3 and 4) was calculated as the deviation of individual pH estimates ( $pH_0$ ) from the mean reconstructed pH across all  $\delta^{11}\text{B}$  measurements. To account for uncertainties, we propagated errors from the  $\delta^{11}\text{B}$  measurements ( $\pm 1\sigma$ ) and temperature ( $\pm 1\text{K}$ ) on  $pK_B$ , yielding  $1\sigma$  error bars for the pH reconstructions.

### 2.2.2. $\delta^{13}\text{C}$ Analytical Methods

Benthic  $\delta^{13}\text{C}$  measurements of *P. ariminensis* were performed on a Thermo Kiel IV Carbonate Device connected to a Thermo MAT 253+ Isotope Ratio Mass Spectrometer at the Paleo<sup>2</sup> Laboratory at the University of Arizona. The  $\delta^{13}\text{C}$  data are reported in permil notation relative to the Vienna Pee Dee Belemnite scale (‰, VPDB). IAEA-603 was analyzed ( $n = 40$ ) as an external standard, and the  $1\sigma$  precision was 0.05‰ for  $^{13}\text{C}$ , which is consistent with the long-term precision of this setup (0.05‰;  $n > 1,500$ ).

### 2.2.3. CFC-11 Interpolation

To characterize the distribution of CFC-11 in the ETNP, we used data from the GLODAPv2 2023 data set (Lauvset et al., 2024). Observational points within the ETNP were filtered for CFC-11 values at depths closest to 500 m, then interpolated across a 2D grid using Ordinary Kriging with a linear variogram model, creating a continuous spatial representation of CFC-11 concentrations (Figure 1b).

## 3. Results

### 3.1. Simulating the ETNP $\Delta^{14}\text{C}$ Anomalies

The ETNP  $\Delta^{14}\text{C}$  anomalies (Lindsay et al., 2016; Marchitto et al., 2007; Rafter et al., 2018, 2019) (Figure 1a) are situated in a “shadow zone” of the geostrophic flow of the North Pacific gyre, where potential vorticity barriers limit exchange between the ETNP and the open Pacific. This hydrodynamic isolation coincides with low oxygen concentrations and weak intrusion of anthropogenic CFC-11 (Figures 1a and 1b), making it a plausible site for localized radiocarbon depletion.

We assess the impact of hydrodynamic isolation using our coupled regional-global box model (Section 2.1), in which we systematically vary the volume of the Marchitto box and its boundary exchange fluxes with the open ocean as simulated by the global CYCLOPS model. Here, we focus on two illustrative end-member scenarios that span a plausible range of conditions: (a) a “fast-flushing” case (red symbols in Figures 3 and 4) with high exchange ( $\sim 5$  Sv) and small volume ( $\sim 5x$  GoC), and (b) a slow-flushing case (yellow symbols in Figures 3 and 4) with low mixing ( $\sim 0.5$  Sv) and larger volume ( $\sim 10x$  GoC). In the Marchitto box, the slow-flushing scenario requires 393 Pg C to match the observed  $\Delta^{14}\text{C}$  anomalies, compared to 1,845 Pg C for the fast-flushing case (Figure 3c). Downstream, inside the GoC, both scenarios converge on  $\sim 600$  Pg C needed to reproduce the  $\Delta^{14}\text{C}$  signals in the GoC subsurface and surface boxes (Figures 3a and 3b). The total carbon added for both end-member scenarios broadly align with the conservative ( $\sim 800$  Pg C) and speculative ( $\sim 2,400$  Pg C) upper bounds from the global radiocarbon budget (Green et al., 2024) (Figure 3a).

The large difference in total carbon released between the two end-member scenarios offers a useful contrast when comparing to reconstructed atmospheric  $\Delta^{14}\text{C}$ ,  $\text{CO}_2$ , and regional pH data. The fast-flushing experiment, which releases 2,482 Pg C, slightly undershoots reconstructed atmospheric  $\Delta^{14}\text{C}$ . This discrepancy is consistent with a possible bias in the simulated  $^{14}\text{C}$  production history before the LGM (Green et al., 2024). Additionally, it overshoots reconstructed  $\text{CO}_2$ , related to the fixed equimolar carbon and alkalinity flux used to match the ETNP  $\Delta^{14}\text{C}$  anomalies. The slow-flushing scenario better fits atmospheric  $\Delta^{14}\text{C}$  and  $\text{CO}_2$ , though both scenarios are broadly consistent with these data considering uncertainties in the  $^{14}\text{C}$  budget and the assumed carbon-to-alkalinity ratio. The similarity in  $\text{CO}_2$  histories across two vastly different carbon cycle scenarios arises because equimolar carbon and alkalinity release have minimal impact on seawater pH, confirmed by the small pH change in our reconstructions for the GoC site (Figures 3f and 4b) based on epifaunal benthic foraminifera.

If the carbon were released as pure  $\text{CO}_2$  without alkalinity, it would lead to substantial local acidification and elevated atmospheric  $\text{CO}_2$  levels. In our slow-flushing scenario, pure  $\text{CO}_2$  addition results in a sustained pH drop of more than 1 unit throughout the deglacial period—far exceeding the minor pH change ( $\sim 0.05$ ) observed in  $\delta^{11}\text{B}$ -derived data (Figure 3f, Figure S1b in Supporting Information S1), which, although lower in temporal resolution than the  $\Delta^{14}\text{C}$  record, shows no evidence of short-term acidification. To generate the observed  $\Delta^{14}\text{C}$  anomalies without deviating from this pH constraint, the geologic carbon must have an alkalinity-to-dissolved inorganic carbon (ALK:DIC) ratio between 1:1 and 1.2:1 (Figure 4b). Pure  $\text{CO}_2$  addition (ALK:DIC of 0:1) immediately drives unobserved acidification before producing any notable  $\Delta^{14}\text{C}$  anomaly. Additionally,  $\text{CO}_2$  addition would cause atmospheric  $\text{CO}_2$  levels to greatly overshoot reconstructed values, reaching approximately 300 ppm by  $\sim 12$ -kyr BP (Figure S1a in Supporting Information S1).

## 4. Discussion

### 4.1. Role of Hydrodynamic Isolation

While geologic carbon release is expected to drive localized  $\Delta^{14}\text{C}$  anomalies, previous attempts to simulate such anomalies in the equatorial and South Pacific have failed, even with carbon release rates comparable to our high-flushing scenario (Ronge et al., 2016; L. Stott et al., 2019; L. D. Stott et al., 2019). To understand this discrepancy,

we consider the carbon isotope mass balance of a region affected by a persistent  $\Delta^{14}\text{C}$  anomaly: First, a larger volume ( $V$ ) of affected water requires more  $^{14}\text{C}$ -free geologic carbon input ( $\Delta C$ ) to attain a given  $\Delta^{14}\text{C}$  anomaly ( $A$ ) against the background seawater DIC. Second, and more importantly, maintaining this anomaly ( $\frac{\delta A}{\delta t} = 0$ ) against mixing ( $M$ ) with the global ocean requires a persistent flux ( $F$ ) of geologic carbon that is reciprocal to the flushing timescale ( $\tau = \frac{V}{M}$ ) of the affected volume, but not the volume itself.

$$\Delta C \approx \frac{-A}{A+1} * V * \text{DIC}$$

$$\frac{\delta A}{\delta t} = 0 = F - \frac{\Delta C}{V} * M = F - \frac{\Delta C}{\tau}$$

$$\int F * \delta t = \Delta C * \frac{\Delta t}{\tau}$$

The key insight from this consideration is that a relatively sizable region of affected water requires a substantial amount of initial carbon release ( $\Delta C$ ) to develop observed anomalies (i.e.,  $A$  of  $-0.2 \approx -200\text{‰}$ ), but the cumulative release needed to sustain these anomalies depends primarily on the flushing timescale. For example, generating a  $\sim 200\%$  anomaly across a 100 m depth interval of the North Pacific thermocline ( $V \approx 8 \times 10^{15} \text{ m}^3$ ) or the GoC ( $V \approx 1.45 \times 10^{14} \text{ m}^3$ ) requires an initial carbon input of 48 Pg C and 0.84 Pg C, respectively. Sustaining these anomalies for 1,000 years against 1 Sv of exchange, however, requires 189 Pg C cumulative release in both cases, as the larger volume is flushed more slowly (254 years) than the smaller one (4.6 years)

Our results demonstrate the observed ETNP  $\Delta^{14}\text{C}$  anomalies can be sustained in a region the size of the GoC, even with relatively short flushing timescales ( $\tau < 5$  years, Figure 4a). In contrast, producing comparable anomalies in a larger region would require decades-long isolation that may be incompatible with known Pacific circulation. These findings suggest that the ETNP shadow zone's reduced ventilation made it uniquely susceptible to sustained  $\Delta^{14}\text{C}$  depletion, consistent with the observed spatial clustering of reconstructed  $\Delta^{14}\text{C}$  anomalies.

Zonal oxygen supply estimates suggest a mean flushing time of 17 years for the eastern tropical Pacific oxygen deficient zones (ODZs north and south of the equator; Sonnerup et al., 2019), and CFC-derived ventilation ages for the ETNP exceed 30 years on the 26.8 isopycnal (Fine et al., 2001). As of 1999, there was a sharp CFC front on the 26.8 isopycnal adjacent to Baja California, with concentrations dropping from  $0.5 \text{ pmol kg}^{-1}$  at 28 N to  $0.1 \text{ pmol kg}^{-1}$  at 24 N (van Geen et al., 2006), placing the Marchitto site and GoC into the most isolated corner of the ETNP shadow zone. Additionally, the reconstructed expansion of the ETNP ODZ during the deglacial period (Ganeshram & Pedersen, 1998; Gardner et al., 1997; Keigwin & Jones, 1990; Lyle et al., 1996; Studer et al., 2021) is consistent with hydrographically restricted oxygen and CFC flow from the subpolar North Pacific to Baja California. This hydrodynamic isolation predisposes the region to develop large  $\Delta^{14}\text{C}$  anomalies, and any deglacial reduction in flushing time would proportionally decrease the required carbon release to drive  $\Delta^{14}\text{C}$  anomalies. This mechanism could plausibly apply also to other ridge-proximal sites with  $\Delta^{14}\text{C}$  anomalies in partially isolated settings, such as the Arabian sea (Bryan et al., 2010) or the North Atlantic under stadial climate conditions (Thornalley et al., 2011, 2015).

Our explanation for the ETNP is in contrast with other Pacific sites where large  $\Delta^{14}\text{C}$  anomalies have been reported without significant isolation from the basin-wide circulation (Bova et al., 2018; Ronge et al., 2016; L. Stott et al., 2009). In these cases, anomalies may be highly localized to the point of carbon release or reflect porewaters within the sediment column. For example, in the case of Galapagos, large  $\Delta^{14}\text{C}$  anomalies in benthic foraminifera (living in the top few centimeters of sediment) coincide with no  $\Delta^{14}\text{C}$  anomalies in nearby deep-sea corals (living on hard seafloor substrates and therefore directly sampling bottom water  $\Delta^{14}\text{C}$ , unlike benthic foraminifera; Chen et al., 2020).

While our optimized release histories appear as stadial- and interstadial-timed millennial-timescale pulses (Figure 3), these should be viewed as schematic outcomes of the optimization rather than literal reconstructions of forcing. The intent of our approach is to bracket the fluxes required under different flushing regimes, not to prescribe climate-paced inputs. More realistically, ridge-related carbon fluxes likely increased more broadly during deglaciation in response to sea-level change (Huybers & Langmuir, 2009; Lund & Asimow, 2011). In our

model ensemble we did not optimize flushing time for a given assumed pulse geologic carbon, but we show that the total amount of carbon release required to meet observed  $\Delta^{14}\text{C}$  anomalies depends critically on regional circulation changes (Figure 4a). As such, we deem it more likely that the millennial-timescale structure of the ETNP  $\Delta^{14}\text{C}$  anomaly responds to changes in regional circulation, rather than reflecting directly the time evolution of the geologic carbon source.

#### 4.2. Carbon Cycle Implications

We find no discernable change in reconstructed seawater pH associated with severe  $\Delta^{14}\text{C}$  anomalies in benthic and planktic foraminifera from the GoC (Figure 4b), consistent with the recent discovery of carbon-rich, pH-neutral and  $\text{CaCO}_3$ -forming hydrothermal vents in the southern GoC (Paduan et al., 2018). The expected regional pH anomaly ( $\Delta\text{pH}$ ) and its effect on seafloor  $\text{CaCO}_3$  saturation ( $\Delta\ln\Omega$ ) depend on the ambient seawater carbonate ion concentration ( $[\text{CO}_3^{2-}]$  of 50–80  $\mu\text{mol kg}^{-1}$ ) and the difference in carbon and alkalinity release fluxes ( $F_{\text{CO}_2}$  minus  $F_{\text{ALK}}$ ) divided by the flushing timescale ( $\tau$ ):

$$2.3 * \Delta\text{pH} \approx \Delta\ln \Omega = \frac{\text{CPF}}{[\text{CO}_3^{2-}]} * \frac{F_{\text{CO}_2} - F_{\text{ALK}}}{\tau}$$

Here, CPF (carbonate proton fraction) equates to the fraction of total seawater buffering due to the bicarbonate/carbonate buffer (Hain et al., 2015). The absence of a pH anomaly or signs of corrosion in our foraminifera samples suggests nearly equimolar  $\text{CO}_2$  and alkalinity fluxes ( $F_{\text{CO}_2} \approx F_{\text{ALK}}$ ; i.e. carbon release predominantly in the form of bicarbonate ion), consistent with the hypothesized “neutralized carbon” release as the source of the ETNP  $\Delta^{14}\text{C}$  anomalies (Green et al., 2024; Rafter et al., 2019).

Once globally dissipated, equimolar carbon and alkalinity release would minimally affect deep-ocean  $\Omega$  and cause only a small atmospheric  $\text{CO}_2$  rise ( $\Delta\ln\text{CO}_2$ ) after accounting for  $\text{CaCO}_3$  compensation:

$$\Delta\ln\text{CO}_2 \approx \frac{0.06\%}{\text{Pmol}} * \left( 2 * \int F_{\text{CO}_2} - \int F_{\text{ALK}} \right)$$

where the scaling factors account for seawater buffering and equilibration with a finite atmosphere (Hain & Sigman, 2024). For example, the cumulative release of 800 Pg geologic carbon as 67 Pmol  $\text{CO}_2$  would cause severe ocean acidification and 67 Pmol net  $\text{CaCO}_3$  dissolution, resulting in an  $\sim 8\%$   $\text{CO}_2$  rise. In contrast, an equimolar  $\text{CO}_2$  and alkalinity release would be pH neutral, cause no  $\text{CaCO}_3$  dissolution, and raise  $\text{CO}_2$  by only 4%, consistent with the +12 ppm  $\text{CO}_2$  rise in our simulated slow-flushing scenario (Figure 3e). Thus, neutralized carbon release can explain the pH-neutral ETNP  $\Delta^{14}\text{C}$  anomalies. Still, even when taken to the likely limit of the global  $^{14}\text{C}$  budget constraint (Green et al., 2024), it would contribute only modestly to the +47% observed deglacial  $\text{CO}_2$  rise. In this scenario,  $\Delta^{14}\text{C}$  anomalies remain concentrated in the ETNP shadow zone, without significantly impacting radiocarbon dating to reconstruct ocean circulation in the rest of the global ocean.

#### 5. Conclusions

Our coupled regional–global box model demonstrates that the large  $\Delta^{14}\text{C}$  anomalies observed in the ETNP during the last deglaciation can be explained by geologic carbon release into a hydrodynamically isolated shadow zone. We show that a cumulative release of  $\sim 800$  Pg of carbon—consistent with global radiocarbon budget constraints—is sufficient to reproduce the anomalies if residence times exceed a few years.

Boron isotope reconstructions from the Gulf of California indicate no corresponding pH anomaly, supporting a pH-neutral, alkalinity-bearing carbon source. Our results suggest that carbon was released primarily as bicarbonate rather than  $\text{CO}_2$ , allowing for both preservation of seafloor carbonate and minimal impact on atmospheric  $\text{CO}_2$ .

These findings reinforce the hypothesis of neutralized geologic carbon release during the deglacial period and demonstrate how regional ocean isolation can amplify local isotopic signals without overprinting the global ocean signal. As such, the ETNP  $\Delta^{14}\text{C}$  anomalies may reflect a localized carbon cycle perturbation that is consistent

with both observational constraints and global mass balance. This supports the continued use of  $\Delta^{14}\text{C}$  as a tracer for global ocean circulation change, provided regional anomalies are carefully considered.

### Conflict of Interest

The authors declare no conflicts of interest relevant to this study.

### Availability Statement

The model code, plotting scripts, model output, and newly compiled  $\delta^{13}\text{C}$ ,  $\Delta^{14}\text{C}$ , and  $\delta^{11}\text{B}$  data used in this study are openly archived on Zenodo at (Green & csun365, 2025) and are also available via GitHub (<https://github.com/RyanAGreen/GoCmodel>).

### Acknowledgments

This research was supported by the National Science Foundation (NSF) through collaborative research Grants OCE-2032343 (to M.P.H.) and OCE-20132340 (to P.A.R.). Additional support was provided by NSF Grants OCE-1636005, AGS-2303599, and OCE-2503657 (to P.A.R.). J.W.B.R. was supported by NERC Grant NE/N011716/1. We thank the Associate Editor as well as Dave Lund and two other anonymous reviewers for their thoughtful comments, which greatly improved this manuscript.

### References

- Barker, S., Greaves, M., & Elderfield, H. (2003). A study of cleaning procedures used for foraminiferal Mg/Ca paleothermometry. *Geochemistry, Geophysics, Geosystems*, 4(9). <https://doi.org/10.1029/2003GC000559>
- Bereiter, B., Eggleston, S., Schmitt, J., Nehrass-Ahles, C., Stocker, T. F., Fischer, H., et al. (2015). Revision of the EPICA Dome C  $\text{CO}_2$  record from 800 to 600 kyr before present. *Geophysical Research Letters*, 42(2), 542–549. <https://doi.org/10.1002/2014GL061957>
- Bereiter, B., Shackleton, S., Baggenstos, D., Kawamura, K., & Severinghaus, J. (2018). Mean global ocean temperatures during the last glacial transition. *Nature*, 553(7686), 39–44. <https://doi.org/10.1038/nature25152>
- Bolin, B. (1960). On the exchange of carbon dioxide between the atmosphere and the sea. *Tellus*, 12(3), 274–281. <https://doi.org/10.3402/tellusa.v12i3.9402>
- Bova, S. C., Herbert, T. D., & Altabet, M. A. (2018). Ventilation of northern and southern sources of aged carbon in the eastern equatorial Pacific during the younger Dryas rise in atmospheric  $\text{CO}_2$ . *Paleoceanography and Paleoclimatology*, 33(11), 1151–1168. <https://doi.org/10.1029/2018PA003386>
- Broecker, W., & Barker, S. (2007). A 190‰ drop in atmosphere's  $\Delta^{14}\text{C}$  during the “Mystery Interval” (17.5 to 14.5 kyr). *Earth and Planetary Science Letters*, 256(1–2), 90–99. <https://doi.org/10.1016/j.epsl.2007.01.015>
- Bryan, S. P., Marchitto, T. M., & Lehman, S. J. (2010). The release of  $^{14}\text{C}$ -depleted carbon from the deep ocean during the last deglaciation: Evidence from the Arabian Sea. *Earth and Planetary Science Letters*, 298(1), 244–254. <https://doi.org/10.1016/j.epsl.2010.08.025>
- Chen, T., Robinson, L. F., Burke, A., Claxton, L., Hain, M. P., Li, T., et al. (2020). Persistently well-ventilated intermediate-depth ocean through the last deglaciation. *Nature Geoscience*, 13(11), 733–738. <https://doi.org/10.1038/s41561-020-0638-6>
- Cook, M. S., & Keigwin, L. D. (2015). Radiocarbon profiles of the NW Pacific from the LGM and deglaciation: Evaluating ventilation metrics and the effect of uncertain surface reservoir ages. *Paleoceanography*, 30(3), 174–195. <https://doi.org/10.1002/2014PA002649>
- Cook, M. S., Keigwin, L. D., Birgel, D., & Hinrichs, K.-U. (2011). Repeated pulses of vertical methane flux recorded in glacial sediments from the southeast Bering Sea. *Paleoceanography*, 26(2), PA2210. <https://doi.org/10.1029/2010PA001993>
- Craig, H. (1957). The natural distribution of radiocarbon and the exchange time of carbon dioxide between atmosphere and sea. *Tellus*, 9(1), 1–17. <https://doi.org/10.3402/tellusa.v9i1.9078>
- Dickson, A. G. (1990). Thermodynamics of the dissociation of boric acid in synthetic seawater from 273.15 to 318.15 K. *Deep-Sea Research, Part A: Oceanographic Research Papers*, 37(5), 755–766. [https://doi.org/10.1016/0198-0149\(90\)90004-F](https://doi.org/10.1016/0198-0149(90)90004-F)
- Fine, R. A., Maillet, K. A., Sullivan, K. F., & Willey, D. (2001). Circulation and ventilation flux of the Pacific Ocean. *Journal of Geophysical Research*, 106(C10), 22159–22178. <https://doi.org/10.1029/1999JC000184>
- Foster, G. L. (2008). Seawater pH,  $\text{pCO}_2$  and  $[\text{CO}_2^*]$  variations in the Caribbean Sea over the last 130 kyr: A boron isotope and B/Ca study of planktic Foraminifera. *Earth and Planetary Science Letters*, 271(1–4), 254–266. <https://doi.org/10.1016/j.epsl.2008.04.015>
- Foster, G. L., Hönisch, B., Paris, G., Dwyer, G. S., Rae, J. W., Elliott, T., et al. (2013). Interlaboratory comparison of boron isotope analyses of boric acid, seawater and marine  $\text{CaCO}_3$  by MC-ICPMS and NTIMS. *Chemical Geology*, 358, 1–14. <https://doi.org/10.1016/j.chemgeo.2013.08.027>
- Frank, M., Eckhardt, J.-D., Eisenhauer, A., Kubik, P. W., Dittrich-Hannen, B., Segl, M., & Mangini, A. (1994). Beryllium 10, thorium 230, and protactinium 231 in Galapagos microplate sediments: Implications of hydrothermal activity and paleoproductivity changes during the last 100,000 years. *Paleoceanography*, 9(4), 559–578. <https://doi.org/10.1029/94PA01132>
- Ganeshram, R. S., & Pedersen, T. F. (1998). Glacial-interglacial variability in upwelling and bioproductivity off NW Mexico: Implications for Quaternary paleoclimate. *Paleoceanography*, 13(6), 634–645. <https://doi.org/10.1029/98PA02508>
- Garcia, H. E., Wang, Z., Bouchard, C., Cross, S. L., Paver, C. R., Reagan, J. R., et al. (2023). World ocean atlas 2023, volume 3: Dissolved oxygen, apparent oxygen utilization, dissolved oxygen saturation and 30-year climate normal. Retrieved from <https://repository.library.noaa.gov/view/noaa/60601>
- Gardner, J. V., Dean, W. E., & Dartnell, P. (1997). Biogenic sedimentation beneath the California Current System for the past 30 kyr and its paleoceanographic significance. *Paleoceanography*, 12(2), 207–225. <https://doi.org/10.1029/96PA03567>
- Gómez-Valdivia, F., Parés-Sierra, A., & Flores-Morales, A. L. (2015). The Mexican coastal current: A subsurface seasonal bridge that connects the tropical and subtropical Northeastern Pacific. *Continental Shelf Research*, 110, 100–107. <https://doi.org/10.1016/j.csr.2015.10.010>
- Green, R. A., & csun365. (2025). RyanAGreen/GoCmodel: v3.0—Full archive: Model, output, and observational data (v3.0) [Software]. Zenodo. <https://doi.org/10.5281/zenodo.15588737>
- Green, R. A., Hain, M. P., & Rafter, P. A. (2024). Deglacial pulse of neutralized carbon from the Pacific seafloor: A natural analog for ocean alkalinity enhancement? *Geophysical Research Letters*, 51(8), e2024GL108271. <https://doi.org/10.1029/2024GL108271>
- Hain, M. P., & Sigman, D. M. (2024).  $\text{CO}_2$  in Earth's ice age cycles. In *Oxford Research Encyclopedia of Climate Science*. <https://doi.org/10.1093/acrefore/9780190228620.013.879>
- Hain, M. P., Sigman, D. M., & Haug, G. H. (2011). Shortcomings of the isolated abyssal reservoir model for deglacial radiocarbon changes in the mid-depth Indo-Pacific Ocean. *Geophysical Research Letters*, 38(4), L04604. <https://doi.org/10.1029/2010GL046158>
- Hain, M. P., Sigman, D. M., & Haug, G. H. (2014). Distinct roles of the Southern Ocean and North Atlantic in the deglacial atmospheric radiocarbon decline. *Earth and Planetary Science Letters*, 394, 198–208. <https://doi.org/10.1016/j.epsl.2014.03.020>

- Hain, M. P., Sigman, D. M., Higgins, J. A., & Haug, G. H. (2015). The effects of secular calcium and magnesium concentration changes on the thermodynamics of seawater acid/base chemistry: Implications for Eocene and Cretaceous ocean carbon chemistry and buffering. *Global Biogeochemical Cycles*, 29(5), 517–533. <https://doi.org/10.1002/2014GB004986>
- Humphreys, M. P., Lewis, E. R., Sharp, J. D., & Pierrot, D. (2021). PyCO2SYS v1.7: Marine carbonate system calculations in Python. *Oceanography*. preprint. <https://doi.org/10.5194/gmd-2021-159>
- Huybers, P., & Langmuir, C. (2009). Feedback between deglaciation, volcanism, and atmospheric CO<sub>2</sub>. *Earth and Planetary Science Letters*, 286(3), 479–491. <https://doi.org/10.1016/j.epsl.2009.07.014>
- Keigwin, L. D., & Jones, G. A. (1990). Deglacial climatic oscillations in the Gulf of California. *Paleoceanography*, 5(6), 1009–1023. <https://doi.org/10.1029/PA005i006p01009>
- Klochko, K., Kaufman, A. J., Yao, W., Byrne, R. H., & Tossell, J. A. (2006). Experimental measurement of boron isotope fractionation in seawater. *Earth and Planetary Science Letters*, 248(1), 276–285. <https://doi.org/10.1016/j.epsl.2006.05.034>
- Lauvset, S. K., Lange, N., Tanhua, T., Bittig, H. C., Olsen, A., Kozyr, A., et al. (2024). The annual update GLODAPv2.2023: The global interior ocean biogeochemical data product. *Earth System Science Data*, 16(4), 2047–2072. <https://doi.org/10.5194/essd-16-2047-2024>
- Lavín, M. F., & Marinone, S. G. (2003). An overview of the physical oceanography of the Gulf of California. In O. U. Velasco Fuentes, J. Sheinbaum, & J. Ochoa (Eds.), *Nonlinear Processes in Geophysical Fluid Dynamics: A tribute to the scientific work of Pedro Ripa* (pp. 173–204). Springer Netherlands. [https://doi.org/10.1007/978-94-010-0074-1\\_11](https://doi.org/10.1007/978-94-010-0074-1_11)
- Lindsay, C. M., Lehman, S. J., Marchitto, T. M., Carriquiry, J. D., & Ortiz, J. D. (2016). New constraints on deglacial marine radiocarbon anomalies from a depth transect near Baja California. *Paleoceanography*, 31(8), 1103–1116. <https://doi.org/10.1002/2015PA002878>
- Lindsay, C. M., Lehman, S. J., Marchitto, T. M., & Ortiz, J. D. (2015). The surface expression of radiocarbon anomalies near Baja California during deglaciation. *Earth and Planetary Science Letters*, 422, 67–74. <https://doi.org/10.1016/j.epsl.2015.04.012>
- Lund, D. C., & Asimow, P. D. (2011). Does sea level influence mid-ocean ridge magmatism on Milankovitch timescales? *Geochemistry, Geophysics, Geosystems*, 12(12), Q12009. <https://doi.org/10.1029/2011GC003693>
- Lund, D. C., Asimow, P. D., Farley, K. A., Rooney, T. O., Seeley, E., Jackson, E. W., & Durham, Z. M. (2016). Enhanced East Pacific rise hydrothermal activity during the last two glacial terminations. *Science*, 351(6272), 478–482. <https://doi.org/10.1126/science.aad4296>
- Lund, D. C., Pavia, F. J., Seeley, E. I., McCart, S. E., Raftar, P. A., Farley, K. A., et al. (2019). Hydrothermal scavenging of <sup>230</sup>Th on the southern East Pacific rise during the last deglaciation. *Earth and Planetary Science Letters*, 510, 64–72. <https://doi.org/10.1016/j.epsl.2018.12.037>
- Lyle, M., Koizumi, I., Richter, C., Fox, P. J., Baldauf, J., & Francis, T. J. (1996). Ocean Drilling Program. Retrieved from [http://www-odp.tamu.edu/publications/prelim/167\\_prel/167prel.pdf](http://www-odp.tamu.edu/publications/prelim/167_prel/167prel.pdf)
- Marchitto, T. M., Lehman, S. J., Ortiz, J. D., Flückiger, J., & Van Geen, A. (2007). Marine radiocarbon evidence for the mechanism of deglacial atmospheric CO<sub>2</sub> rise. *Science*, 316(5830), 1456–1459. <https://doi.org/10.1126/science.1138679>
- Nix, R. K. (2013). *The Gulf of California. A physical, geological and biological study*. University of Texas. Retrieved from <https://citeseerx.ist.psu.edu/document?repid=rep1&type=pdf&doi=4fda34a7425758aa17c3d0035676f87db6f9f11>
- Paduan, J. B., Zierenberg, R. A., Clague, D. A., Spelz, R. M., Caress, D. W., Troni, G., et al. (2018). Discovery of hydrothermal vent fields on Alarcón Rise and in Southern Pescadero Basin, Gulf of California. *Geochemistry, Geophysics, Geosystems*, 19(12), 4788–4819. <https://doi.org/10.1029/2018GC007771>
- Rae, J. W. B. (2018). Boron isotopes in foraminifera: Systematics, biomineralisation, and CO<sub>2</sub> reconstruction. In H. Marschall & G. Foster (Eds.), *Boron Isotopes* (pp. 107–143). Springer International Publishing. [https://doi.org/10.1007/978-3-319-64666-4\\_5](https://doi.org/10.1007/978-3-319-64666-4_5)
- Rae, J. W. B., Foster, G. L., Schmidt, D. N., & Elliott, T. (2011). Boron isotopes and B/Ca in benthic foraminifera: Proxies for the deep ocean carbonate system. *Earth and Planetary Science Letters*, 302(3–4), 403–413. <https://doi.org/10.1016/j.epsl.2010.12.034>
- Raftar, P. A., Carriquiry, J. D., Herguera, J., Hain, M. P., Solomon, E. A., & Southon, J. R. (2019). Anomalous > 2000-year-old surface ocean radiocarbon age as evidence for deglacial geologic carbon release. *Geophysical Research Letters*, 46(23), 13950–13960. <https://doi.org/10.1029/2019GL085102>
- Raftar, P. A., Gray, W. R., Hines, S. K. V., Burke, A., Costa, K. M., Gottschalk, J., et al. (2022). Global reorganization of deep-sea circulation and carbon storage after the last ice age. *Science Advances*, 8(46), eabq5434. <https://doi.org/10.1126/sciadv.abq5434>
- Raftar, P. A., Hain, M. P., Arellano-Torres, E., Kaustubh, T., Tappa, E. J., Machain Castillo, M.-L., et al. (2026). Spatial and temporal variability of eastern Pacific radiocarbon and carbon chemistry from the ice age to today. *Paleoceanography and Paleoclimatology*. <https://doi.org/10.1029/2025PA005265>
- Raftar, P. A., Herguera, J.-C., & Southon, J. R. (2018). Extreme lowering of deglacial seawater radiocarbon recorded by both epifaunal and infaunal benthic Foraminifera in a wood-dated sediment core. *Climate of the Past*, 14(12), 1977–1989. <https://doi.org/10.5194/cp-14-1977-2018>
- Reimer, P. J., Austin, W. E. N., Bard, E., Bayliss, A., Blackwell, P. G., Ramsey, C. B., et al. (2020). The IntCal20 Northern Hemisphere radiocarbon age calibration curve (0–55 cal kBP). *Radiocarbon*, 62(4), 725–757. <https://doi.org/10.1017/RDC.2020.41>
- Revelle, R., & Suess, H. E. (1957). Carbon dioxide exchange between atmosphere and ocean and the question of an increase of atmospheric CO<sub>2</sub> during the past decades. *Tellus*, 9(1), 18–27. <https://doi.org/10.1111/j.2153-3490.1957.tb01849.x>
- Ronge, T. A., Tiedemann, R., Lamy, F., Köhler, P., Alloway, B. V., De Pol-Holz, R., et al. (2016). Radiocarbon constraints on the extent and evolution of the South Pacific glacial carbon pool. *Nature Communications*, 7(1), 11487. <https://doi.org/10.1038/ncomms11487>
- Skinner, L. C., Fallon, S., Waelbroeck, C., Michel, E., & Barker, S. (2010). Ventilation of the deep Southern Ocean and deglacial CO<sub>2</sub> rise. *Science*, 328(5982), 1147–1151. <https://doi.org/10.1126/science.1183627>
- Sonnerup, R. E., Chang, B. X., Warner, M. J., & Mordy, C. W. (2019). Timescales of ventilation and consumption of oxygen and fixed nitrogen in the eastern tropical South Pacific oxygen deficient zone from transient tracers. *Deep Sea Research Part I: Oceanographic Research Papers*, 151, 103080. <https://doi.org/10.1016/j.dsr.2019.103080>
- Stott, L., Davy, B., Shao, J., Coffin, R., Pecher, I., Neil, H., et al. (2019). CO<sub>2</sub> release from pockmarks on the Chatham rise-bounty trough at the glacial termination. *Paleoceanography and Paleoclimatology*, 34(11), 1726–1743. <https://doi.org/10.1029/2019PA003674>
- Stott, L., Southon, J., Timmermann, A., & Koutavas, A. (2009). Radiocarbon age anomaly at intermediate water depth in the Pacific Ocean during the last deglaciation. *Paleoceanography*, 24(2). <https://doi.org/10.1029/2008PA001690>
- Stott, L., & Timmermann, A. (2011). Hypothesized link between glacial/interglacial atmospheric CO<sub>2</sub> cycles and storage/release of CO<sub>2</sub>-rich fluids from deep-sea sediments. In H. Rashid, L. Polyak, & E. Mosley-Thompson (Eds.), *Geophysical Monograph Series* (Vol. 193, pp. 123–138). American Geophysical Union. <https://doi.org/10.1029/2010GM001052>
- Stott, L. D., Harazin, K. M., & Krupinski, N. B. Q. (2019). Hydrothermal carbon release to the ocean and atmosphere from the eastern equatorial Pacific during the last glacial termination. *Environmental Research Letters*, 14(2), 025007. <https://doi.org/10.1088/1748-9326/aafe28>

- Studer, A. S., Mekik, F., Ren, H., Hain, M. P., Oleynik, S., Martínez-García, A., et al. (2021). Ice age-holocene similarity of foraminifera-bound nitrogen isotope ratios in the eastern equatorial Pacific. *Paleoceanography and Paleoclimatology*, 36(5), e2020PA004063. <https://doi.org/10.1029/2020PA004063>
- Stuiver, M., & Polach, H. A. (1977). Discussion reporting of  $^{14}\text{C}$  data. *Radiocarbon*, 19(3), 355–363. <https://doi.org/10.1017/S0033822200003672>
- Thornalley, D. J. R., Barker, S., Broecker, W. S., Elderfield, H., & McCave, I. N. (2011). The deglacial evolution of North Atlantic deep convection. *Science*, 331(6014), 202–205. <https://doi.org/10.1126/science.1196812>
- Thornalley, D. J. R., Bauch, H. A., Gebbie, G., Guo, W., Ziegler, M., Bernasconi, S. M., et al. (2015). A warm and poorly ventilated deep Arctic Mediterranean during the last glacial period. *Science*, 349(6249), 706–710. <https://doi.org/10.1126/science.aaa9554>
- Trudgill, M., Nuber, S., Block, H. E., Crumpton-Banks, J., Jurikova, H., Little, E., et al. (2024). A simple, low-blank batch purification method for high-precision boron isotope analysis. *Geochemistry, Geophysics, Geosystems*, 25(3), e2023GC011350. <https://doi.org/10.1029/2023GC011350>
- van Geen, A., Smethie, W. M., Jr., Horneman, A., & Lee, H. (2006). Sensitivity of the North Pacific oxygen minimum zone to changes in ocean circulation: A simple model calibrated by chlorofluorocarbons. *Journal of Geophysical Research*, 111(C10), C10004. <https://doi.org/10.1029/2005JC003192>
- Virtanen, P., Gommers, R., Oliphant, T. E., Haberland, M., Reddy, T., Cournapeau, D., et al. (2020). SciPy 1.0: Fundamental algorithms for scientific computing in Python. *Nature Methods*, 17(3), 261–272. <https://doi.org/10.1038/s41592-019-0686-2>
- Vogl, J., & Rosner, M. (2012). Production and certification of a unique set of isotope and delta reference materials for boron isotope determination in geochemical, environmental and industrial materials. *Geostandards and Geoanalytical Research*, 36(2), 161–175. <https://doi.org/10.1111/j.1751-908X.2011.00136.x>
- Xu, C., Jurikova, H., Nuber, S., Steele, R. C. J., Trudgill, M., Barker, S., et al. (2024). A rapid, simple, and low-blank pumped ion-exchange column chromatography technique for boron purification from carbonate and seawater matrices. *Geochemistry, Geophysics, Geosystems*, 25(2), e2023GC011228. <https://doi.org/10.1029/2023GC011228>
- Zeebe, R. E., & Wolf-Gladrow, D. (2001). *CO<sub>2</sub> in seawater: Equilibrium, kinetics, isotopes* (Vol. 65). Gulf Professional Publishing. Retrieved from <https://books.google.com/books?hl=en&lr=&id=g3j3Zn4kEscC&oi=fnd&pg=PA1&dq=wolf+gladorw+zeebe&ots=ldTvKYtkyP&sig=gg0lC0nb84SxhMjD0kRvvMvnPH8>